Controlling oxide surface dipole and reactivity with intrinsic nonstoichiometric epitaxial reconstructions

Seungchul Kim, Ofer Sinai, Chan-Woo Lee, and Andrew M. Rappe

Controlling Oxide Surface Dipole and Reactivity with Intrinsic Nonstoichiometric Epitaxial Reconstructions

Seungchul Kim,[1,2] Ofer Sinai,[3] Chan-Woo Lee,[2] and Andrew M. Rappe[2,*]

[1]Center for Computational Science, Korea Institute of Science and Technology, Seoul 136-791, Republic of Korea
[2]The Makineni Theoretical Laboratories, Department of Chemistry,
University of Pennsylvania, Philadelphia, PA 19104-6323, USA
[3]Department of Materials and Interfaces, Weizmann Institute of Science, Rehovoth 76100, Israel
(Dated: November 25, 2015)

The composition and reconstruction of oxide surfaces can be deterministically controlled via ambient conditions. We demonstrate that such intrinsic alterations can have a crucial effect on the surface dipole and reactivity, even for surfaces with the same crystallographic plane. The surface dipole potential drops of $BaTiO_3$, $SrTiO_3$, $LaFeO_3$ and TiO_2 surfaces with various reconstructions and compositions are shown to vary by as much as 5 V, leading to significant variation of the band edge positions at these surfaces. These variations are shown to correlate with the calculated oxygen binding energy, demonstrating how oxide surface reactivity can be substantially manipulated using environmental changes.

I. INTRODUCTION

The surface dipole is an important property of semiconductor surfaces, playing a critical role in electron transfer phenomena. Along with long-range band-bending, it determines the amount of energy involved in electron transfer between a semiconductor and the vacuum, and thus strongly affects the overall surface work function. This energy alignment influences electronic phenomena at heterogeneous interfaces including Schottky barriers[1], contact potentials[2], electron transfer at electrodes of electrochemical cells and photocatalysts, and interaction between substrates and adsorbed molecules[3].

The work function is highly dependent on the details of the surface and its environment, as demonstrated by its known dependence on crystallographic orientation[4–6], pressure/temperature[7–13] and pH of solution[14,15], interaction with adjacent solvents[16], and surface molecular physisorption[17,18] and chemisorption[19].

We expect that surface effects are especially important for oxides since their surface compositions and structures can be significantly changed depending on the environmental conditions to which they are exposed or in which they are prepared[12,20–26]. In particular, the surface atomic geometry can be very different from that of the bulk-like surface due to reconstruction, even though the crystallographic orientation of the surface is unchanged. While such changes are known to affect the surface work function, e.g. in SnO_2[12], the subsequent changes in the surface's photocatalytic behavior were only recently examined for low-index surfaces of Cu_2O[6] and $SrTiO_3$[27], and have not often been considered in other studies.

Environmentally-driven changes in oxide surfaces are also important from a technological viewpoint due to, for instance, potential applications to solar-to-chemical energy conversion by photocatalytic water splitting and CO$_2$ hydrogenation[28–30]. As photocatalysts are often exposed to harsh chemical conditions, the surface structure might be different from that under mild conditions. Furthermore, environmental conditions can be intentionally manipulated to produce desired surface structures[12,20,22]. Such changes may significantly affect surface band structure and energetics (see Ref. 31 for a recent example). It is therefore important to gauge the full extent to which environmentally-driven morphological changes to oxide surfaces can affect their properties and behavior.

In this study, we use first principles calculations to investigate these questions, focusing on surface dipoles and chemical reactivity. We demonstrate that compositional or structural changes to surfaces of the same material can alter the surface potential drop by multiple volts, even though the surfaces compared *share an identical crystallographic orientation*. These results imply that environmentally-driven structural changes to a given oxide surface can be used as powerful tools to tailor its reactivity. Moreover, because these changes are *intrinsic*, *i.e.* no additional material is involved – they need not incur the undesirable side effects that extrinsic surface modifications may have, such as blocking of catalytic sites by molecular overlayers.

II. METHODS

We investigate four metal oxides. Barium titanate ($BaTiO_3$, BTO) and lanthanum ferrite ($LaFeO_3$, LFO) were chosen because their surfaces have various observed atomic compositions[20,32,33]. Strontium titanate ($SrTiO_3$, STO) was chosen to examine the geometric effect using its compositionally identical but geometrically different structures (*i.e.* various TiO_2 double layer (DL) structures)[21,34]. Rutile (TiO_2)[35] was chosen due to its potential applications to solar-to-chemical energy conversion technology. All structures have been modeled theoreti-

cally or observed experimentally. Geometric structures are displayed in Ref. 20 for BTO, in Ref. 21 for STO, and in Ref. 35 for TiO_2, as well as in the Appendix. The surfaces were modeled using slabs with identical top and bottom surfaces in periodic supercells (Fig. 1). Seven-unit cell-thick (≈ 28 Å) slabs were used for ABO_3 structures, with the atoms in the centermost three unit cells (≈ 12 Å) fixed during structural relaxation (Fig. 1). For rutile structures, four-unit cell-thick (≈ 26 Å) slabs were used, with atoms in the centermost one and a half unit cells (≈ 9 Å) fixed.

Density functional theory (DFT) calculations were carried out using plane-wave basis set total energy calculations[36], as implemented in Quantum-ESPRESSO[37], with optimized norm-conserving pseudopotentials[38,39]. Hellman-Feynman forces from the generalized gradient approximation (GGA-PBE)[40] were used to relax the atomic structures via the BFGS algorithm[41–45] with a 0.01 eV/Å threshold for convergence. The linear response GGA+U method[46] was used for electronic structure calculations. The $3d$ Hubbard U values of Ti and Fe are 4.86 eV (BTO), 4.72 eV (STO), 4.82 eV (TiO_2) and 4.40 eV (LFO). Dense $6 \times 6 \times 1$ and $3 \times 8 \times 1$ k-point grids were used for the atomic structure relaxation of the 1×1 surface cells of ABO_3 and rutile, respectively, while $12 \times 12 \times 1$ and $6 \times 16 \times 1$ grids were used for calculations of the electronic structure. A 50 Ry plane-wave cutoff was used. All vacuum-relative band edges were converged to within 0.1 eV with respect to the computational parameters.

III. RESULTS AND DISCUSSION

A. Surface structure-dependent electric dipole

The surface dipole is associated with a potential drop across the surface of $4\pi p_z/A$, where p_z is the surface dipole moment and A is the surface area. First, we ex-
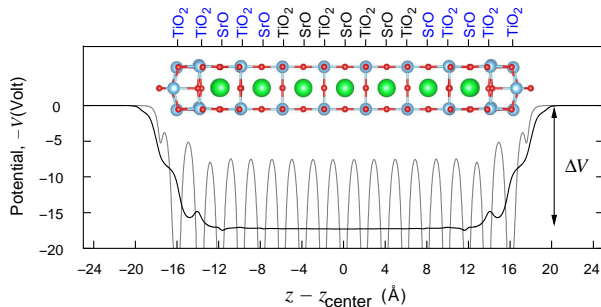

FIG. 1: (Color online) Graphical depiction of atomic model (SrTiO$_3$ 2×1 DL) and the method of determining ΔV. The gray and black curves are the microscopic and macroscopic electrostatic potential, respectively. Atoms in the two unit cells near the surfaces (blue labels) were relaxed, while seven center layers (black labels) were fixed.
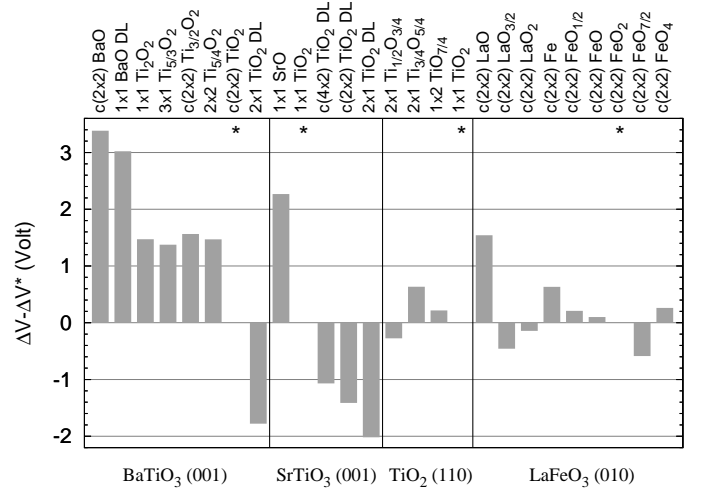

FIG. 2: Macroscopic electrostatic potential change across the surface (ΔV) relative to ΔV of the relevant bulk-terminated surface (marked by *). The stoichiometries in the figure are the atomic composition in the 1×1 cell for BTO, STO and LFO, and in the half-unit cell for TiO_2. DL = double layer.

amine changes in this potential drop as the surface undergoes structural and compositional deformations. We define ΔV as the change in the macroscopic electrostatic potential from the center of the slab (V_{center}^{slab}) to the vacuum (V_{vac}^{slab}), $\Delta V \equiv V_{vac}^{slab} - V_{center}^{slab}$ (Fig. 1). A more negative value of ΔV represents a greater barrier for electrons to escape to vacuum. Taking ΔV of a bulk-like termination as reference in each material, we examine in Fig. 2 the variation in ΔV in all systems.

We find a strong dependence of the surface dipole on its termination. Remarkably, the magnitude of change in ΔV is far greater than that due to changes in pH (0.059 V per pH)[15] or oxygen partial pressure[7–10]. For instance, the dipole potential drop differs as much as 5.16 V between the BaO and TiO_2 DL terminations of BTO. We find three trends in the behavior of the surface dipole: first, surface oxidation induces more negative ΔV than less oxidized compositions; second, A-rich surfaces of ABO_3 have more positive potential drops than B-rich surfaces; and third, surfaces with oxygen ions farther away from the bulk display more negative ΔV.

These trends can be understood by the fact that even though the materials are non-polar, deformation near the surface causes the appearance of surface dipole layers. As the surface oxidizes, oxygen-rich reconstructions are favored, bringing negative charge to the surface, and making near-surface ions more positive. This is expressed as an added dipole moment pointing *into* the surface, leading to a more negative potential drop across it. Specifically, in Fig. 2, the calculated surface potential drops of BTO, TiO_2 and LFO surface reconstructions follow this trend. This is consistent with previous observations that the work functions of oxides increase as the oxygen partial pressure increases.[7–11] However, this correlation does not extend to highly cation- or oxygen-rich surfaces,
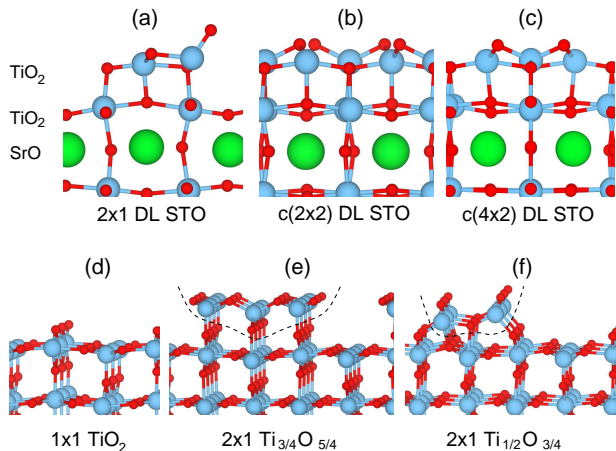
FIG. 3: (Color online) Side view of (a–c) TiO_2 double-layer structures of $SrTiO_3$ (001) and (d–f) reconstructed rutile (110). (d) is a bulk-like termination whose composition is Ti_2O_4 in a 1×1 unit cell. In (e) and (f), Ti_3O_5 and Ti_2O_3 over-layers (dotted line) were adhered onto the bulk-like 2×1 termination.

for which some of ions are more neutral. For instance, the oxygen atoms on $c(2 \times 2)$ $FeO_{7/2}$ of LFO are anionic, while the additional surface oxygen species are neutral on the more oxygen-rich surface, $c(2 \times 2)$ FeO_4. The O-O bond lengths on the $c(2 \times 2)$ FeO_4 surface are almost the same as those of O_2 gas[47].

The finding that A-rich surfaces have smaller *into*-surface dipoles than B-rich surfaces can be explained by the higher electron affinity of the BO_2 layer relative to the AO layer. For bulk-like terminations, the outermost BO_2 layer of the BO_2-termination will accept electrons from the subsurface AO layer, while the AO surface layer of the AO-termination will donate electrons to the BO_2 subsurface layer. For example, a calculation of the ionization energy of a single isolated layer of BaO yields a result of 3.09 eV, while the electron affinity of an isolated TiO_2 layer is 4.04 eV, indicating that electron transfer must occur from BaO to TiO_2 layers in BTO. Furthermore, an examination of the real-space charge density of BTO shows greater subsurface-to-surface charge transfer to a TiO_2-terminated surface than to a BaO-terminated one (see Appendix). Since the same phenomenon is observed for STO and LFO, it is highly probable that more negative potential drops across BO_2 terminated surfaces are a general trend among ABO_3 materials.

The processes leading to the observed overall dipole changes can be complex. To demonstrate this, we first draw attention to a remarkable trend observed in three TiO_2 DL structures of STO, namely 2×1 DL, $c(2 \times 2)$ DL and $c(4 \times 2)$ DL (see Fig. 3). The potential drops across these structures are substantially different from one another despite having exactly the same layer-by-layer compositions[21]. This variation in ΔV is dominated by the the potential drop across the over-layer (Table I). In the 2×1 structure, the over-layer possesses a stronger

		$\Delta V - \Delta V^*$	$\Delta \Delta V_D$	ΔV_{OL}	ΔV_e
$SrTiO_3$	2×1	2.02	-0.40	2.63	-0.22
$SrTiO_3$	$c(2 \times 2)$	1.37	-0.22	1.82	-0.23
$SrTiO_3$	$c(4 \times 2)$	1.07	-0.26	1.89	-0.56
TiO_2	2×1 $Ti_{3/4}O_{5/4}$	-0.63	2.52	1.34	-4.49
TiO_2	2×1 $Ti_{1/2}O_{3/4}$	0.27	2.54	1.92	-4.18

TABLE I: Decomposition of the overall change in ΔV relative to the bulk-terminated surface, $\Delta V - \Delta V^*$, in $SrTiO_3$ and TiO_2 surface reconstructions.

electric dipole pointing into the surface, due to the location of oxygen anions higher (out toward the vacuum) than on the other surfaces.

To analyze this geometric effect of the over-layer geometry, we decomposed the over-layer adhesion process into three steps. First, a bulk-like substrate deforms to the structure it will adopt when the over-layer adheres. We denote the resulting change in the potential drop by $\Delta \Delta V_D$. Second, the over-layer is mounted on the deformed substrate. We denote the potential drop associated with the isolated over-layer by ΔV_{OL}. And third, the electrons redistribute to form chemical bonds between the substrate and over-layer. This redistribution is associated with a potential change ΔV_e. Thus, the overall change in the surface potential drop from the bulk-like surface (ΔV^*) to the relaxed surface with outer layer (ΔV) is expressed as

$$\Delta V - \Delta V^* = \Delta \Delta V_D + \Delta V_{OL} + \Delta V_e \quad (1)$$

The values found for these parameters for each of the three TiO_2 double-layer structures of $SrTiO_3$, as well as the two reduced 2×1 surfaces of rutile TiO_2, are collected in Table I. In $SrTiO_3$, it is evident that ΔV_{OL} of the 2×1 surface is much larger than ΔV_{OL} of the other two structures, indicating that the geometry of the over-layer largely determines the overall surface dipole. In rutile TiO_2, a similar geometric effect is observed. Despite being less oxidized, rutile $Ti_{1/2}O_{3/4}$ displays the more negative potential drop. This is caused mainly because of the dipole moment of the over-layer, which is adhered onto the bulk-like TiO_2 termination (See Fig. 3). ΔV_e and $\Delta \Delta V_D$ are very large but comparable in both these structures, so that they amount to only a minor enhancement of the difference between them.

The interplay of effects leading to the overall observed dipole is also evident in the finding that while in BTO, geometry changes to the dipole upon surface reduction tend to enhance changes due to electronic redistribution, in TiO_2 and LFO they tend to counteract them. The TiO_2-terminated BTO surface is reduced by introducing Ti ions on top of Ba ions (Fig. 7). Such Ti ions are located higher (toward the vacuum) than other ions on the surface, leading to a large change in ΔV for *e.g.* the 2×2 $Ti_{5/4}O_2$ reconstruction (Fig. 2). On the 1×2 $TiO_{7/4}$ reduced surface of rutile, the dipole change due to the

presence of Ti^{3+} ions (which are found adjacent to O vacancies at the surface) is mitigated by upward relaxation of the O ions underneath them. Finally, upon reduction of FeO_2-terminated LFO to FeO, the O ions removed are those which are lower than the surface Fe ions, leading to a relatively minor change in ΔV.

B. Variations in band edges

Our finding of large variations in the surface dipole must play an important role in any surface phenomenon that is related to the level alignment. For example, the potential usefulness of such surfaces as photocatalysts for water splitting or CO_2 hydrogenation can be determined by comparing the valence band maximum (VBM) and the conduction band minimum (CBM) with the redox potentials of the half reactions. In particular, for photocatalytic water splitting, the CBM of the photocatalyst must be higher than the H^+/H_2 redox potential, and the VBM must be lower than the O_2/H_2O redox potential[29,30].

In order to provide a useful estimation of surface reactivity, the VBM and CBM must be determined relative to the vacuum energy (eV_{vac}^{slab}, where $e < 0$ is the electron charge). To achieve this, we proceed as follows. We invoke first the concept of the band gap center (BGC $\equiv$ (VBM + CBM)/2)[48]. Following Perdew and Levy's theorem[49], the BGC is predicted by the exact DFT exchange-correlation functional as the average of the Kohn-Sham eigenvalues of the highest occupied (ϵ_N) and lowest unoccupied states (ϵ_{N+1}). These are the derivatives of total energy with respect to the number of electrons in an N-electron system (*i.e.* $\epsilon_N = \partial E/\partial M|_{M \to N-\delta}$, $\epsilon_{N+1} = \partial E/\partial M|_{M \to N+\delta}$)[49,50]. Because the Hubbard U in the linear response GGA+U method is determined so that it removes the spurious curvature and improves the slope of the total energy as a function of the number of electrons in the GGA formalism[46], it is expected to provide a more reliable estimate of the BGC than GGA.

Excluding long range band bending (ΔV_{bb}), V_{center}^{slab} in a sufficiently thick slab may be assumed to match the bulk electrostatic potential (V^{bulk})[51]. The potential change from deep bulk to vacuum is thus

$$V_{vac}^{slab} - V^{bulk} = \Delta V + \Delta V_{bb}, \qquad (2)$$

where $\Delta V_{bb} \equiv V_{center}^{slab} - V^{bulk}$. The vacuum-relative BGC is therefore

$$BGC = \{BGC - eV^{bulk}\} - e(\Delta V + \Delta V_{bb}), \qquad (3)$$

where $\{BGC - eV^{bulk}\}$, the value of the BGC relative to the average electrostatic potential far from any surface, is obtained from a bulk single-crystal DFT+U calculation. The vacuum-relative VBM and CBM are then

determined as

$$CBM \equiv BGC + \frac{1}{2}\Delta_{exp} \qquad (4)$$

$$VBM \equiv BGC - \frac{1}{2}\Delta_{exp}, \qquad (5)$$

where Δ_{exp} is the experimental band gap.

The value of ΔV_{bb} is dependent on the interplay of surface and bulk states[52]. It is however possible to bound it by considering limiting cases. In the Schottky limit, no gap states are induced at the surface and $\Delta V_{bb} = 0$. In the Bardeen limit, a high density of surface states "pins" the Fermi level (E_F) to a surface-determined energy[53], such that E_F is known relative to eV_{vac}^{slab}. Given the bulk doping level, the position of E_F in the gap can be derived semiclassically[54] (in this work we take the bulk to be undoped), immediately yielding the bulk VBM and CBM relative to eV_{vac}^{slab}.

The band edges resulting from this procedure are shown in Fig. 4. For metallic surfaces full "pinning" is assumed; otherwise both "pinned" and "unpinned" limits are shown. The redox potentials of some technologically relevant photocatalytic reactions are also shown on the same scale, demonstrating the importance of intrinsic surface structural changes for tailoring the surface reactivity. Note that beyond the ΔV and ΔV_{bb} potential drops we have considered, band edges may change further due to solvent effects such as pH change, a Helmholtz layer dipole[55], or charge transfer to/from the solvent[16].

C. Correlation of the BGC with the binding energy of reactants

As a further demonstration, we compare oxygen evolution reactions (OERs) on STO, BTO, and TiO_2 surfaces. OERs are regarded as key reactions for hydrogen production. The binding energy of the oxygen atom (ΔE_O) has been identified as a descriptor for the reaction, *i.e.* the catalytic activity of OERs on an oxide catalyst can be predicted from ΔE_O on that catalyst[56,57]. The oxygen binding energy is defined by the following reaction:

$$H_2O_{(g)} + * + \Delta E_O \to H_{2(g)} + O^*_{(ads)}, \qquad (6)$$
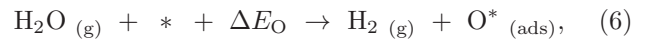
where * is an active site on the surface.

Fig. 5 shows ΔE_O on neutral and oxidized surfaces of titanates as a function of the BGC. We find that ΔE_O can be shifted more than 1 eV by changing of surface reconstruction. This can have a substantial effect on OERs; Rossmeisl *et al.* have predicted that a 1 eV difference in ΔE_O can change the overpotential for rutile-type oxide catalysts by 0.36 - 0.64 V[57]. In particular, the fact that the STO 2×1 TiO_2 DL structure exhibits smaller ΔE_O than the 1×1 TiO_2 agrees with the recent finding that the former catalyzes OERs more efficiently[27]. Furthermore, ΔE_O is roughly proportional to the BGC (Fig. 5), and thus should also be correlated to the overpotential of
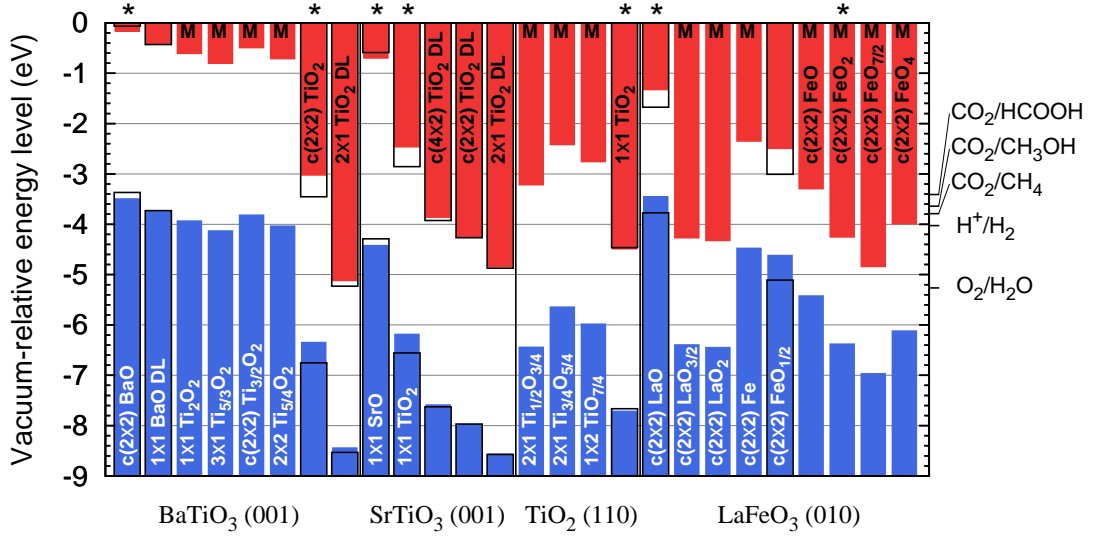
FIG. 4: (Color online) Vacuum-relative band edges in the full Fermi level pinning limit (full bars) and the non-pinning limit (hollow bars) where relevant. $\star$ denotes bulk-like terminations, and M denotes metallic surface terminations. The reducing potentials[48] of CO_2, H^+ and O_2 at pH 7 are shown on the right axis.
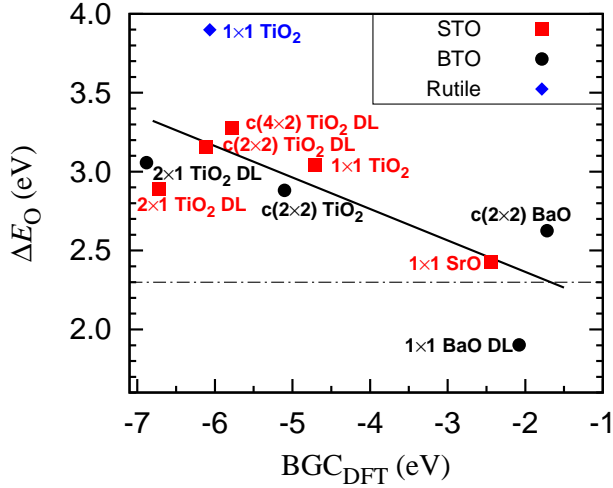

FIG. 5: (Color online) Correlation of the BGC ($\Delta V_{bb} = 0$) of neutral and oxidized nonmetallic surfaces with ΔE_O of those surfaces. The dot-dashed line is the optimal ΔE_O for OER on rutile-type oxides, as determined in Ref. 57. The solid black line shows a linear fit of the data (slope = 0.20±0.06).

OERs. Thus, the catalytic activity of oxide surfaces can be controlled by environmentally-induced, intrinsic surface restructuring, with the BGC serving as an important guideline.

IV. CONCLUSION

We have demonstrated that the intrinsic surface stoichiometry and structure plays a vital role in determining the dipoles and reactivity of oxide surfaces, even if crystallographic orientation is unaltered and without invoking extrinsic adsorbates. Our study shows that electron transfer phenomena can be better understood by considering detailed surface structures: the extent of oxidation, the cation termination, and the relative heights of anions and cations combine to shift the positions of the VBM and CBM. Considering surface structure is especially important when oxides are exposed to extreme operating conditions such as highly reducing/oxidizing conditions for photocatalysts, electrolytic cells, and fuel cells. Furthermore, we have shown that the position of the band gap center guides how the surface should be manipulated to improve catalytic performance.

V. ACKNOWLEDGMENTS

[*] corresponding author: rappe@sas.upenn.edu

[1] C. Kittel, *Introduction to Solid State Physics* (JohnWiley & Sons, Inc., 1996), chap. 19, pp. 570–576, 7th ed.

[2] N. W. Ashcroft and N. D. Mermin, *Solid State Physics* (Harcourt College Publishers, 1976), chap. 18, pp. 360–362.

[3] M. T. Greiner, M. G. Helander, W.-M. Tang, Z.-B. Wang, J. Qiu, and Z.-H. Lu, Nat. Mater. **11**, 76 (2012).

[4] N. D. Lang and W. Kohn, Phys. Rev. B **3**, 1215 (1971).

[5] L. F. Zagonel, M. Baurer, A. Bailly, O. Renault, M. Hoffmann, S.-J. Shih, D. Cockayne, and N. Barrett, J. Phys.: Condens. Matter **21**, 314013 (2009).

[6] L. I. Bendavid and E. A. Carter, J. Phys. Chem. B **117**, 15750 (2013).

[7] S. Badwal, T. Bak, S. Jiang, J. Love, J. Nowotny, M. Rekas, C. Sorrell, and E. Vance, J. Phys. Chem. Solids **62**, 723 (2001).

[8] T. Bak, J. Nowotny, M. Rekas, and C. Sorrell, J. Phys. Chem. Solid **62**, 731 (2001).

[9] T. Bak, J. Nowotny, M. Rekas, and C. Sorrell, J. Phys. Chem. Solid **62**, 737 (2001).

[10] D. F. Cox, T. B. Fryberger, and S. Semancik, Phys. Rev. B **38**, 2072 (1988).

[11] V. E. Henrich, Rep. Prog. Phys. **48**, 1481 (1985).

[12] E. De Frésart, J. Darville, and J. Gilles, Appl. Surf. Sci. **11-12**, 637 (1982).

[13] I. M. Vitomirov, A. Raisanen, A. C. Finnefrock, R. E. Viturro, L. J. Brillson, P. D. Kirchner, G. D. Pettit, and J. M. Woodall, Phys. Rev. B **46**, 13293 (1992).

[14] Y. Matsumoto and E. Sato, Mater. Chem. Phys. **14**, 397 (1986).

[15] J. M. Bolts and M. S. Wrighton, J. Phys. Chem. **80**, 2641 (1976).

[16] M. G. Kibria, S. Zhao, F. A. Chowdhury, Q. Wang, H. P. T. Nguyen, M. L. Trudeau, H. Guo, and Z. Mi, Nat. Commun. **5**, 3825 (2014).

[17] M.-L. Bocquet, A. M. Rappe, and H.-L. Dai, Mol. Phys. **103**, 883 (2005).

[18] Y. Zhou, C. Fuentes-Hernandez, J. Shim, J. Meyer, A. J. Giordano, H. Li, P. Winget, T. Papadopoulos, H. Cheun, J. Kim, et al., Science **336**, 327 (2012).

[19] T. C. Leung, C. L. Kao, and W. S. Su, Phys. Rev. B **68**, 195408 (2003).

[20] A. M. Kolpak, D. Li, R. Shao, A. M. Rappe, and D. A. Bonnell, Phys. Rev. Lett. **101**, 036102 (2008).

[21] O. Warschkow, M. Asta, N. Erdman, K. Poeppelmeier, D. Ellis, and L. Marks, Surf. Sci. **573**, 446 (2004).

[22] B. Stanka, W. Hebenstreit, U. Diebold, and S. Chambers, Surf. Sci. **448**, 49 (2000).

[23] V. E. Henrich and P. A. Cox, *The Surface Science of Metal Oxides* (Cambridge University Press, 1994), chap. 2, pp. 14 – 63.

[24] D. A. Bonnell, J. Am. Ceram. Soc. **81**, 3049 (1998).

[25] G. S. Rohrer, V. E. Henrich, and D. A. Bonnell, Science **250**, 1239 (1990).

[26] E. De Frésart, J. Darville, and J. M. Gilles, Solid State Commun. **37**, 13 (1981).

[27] J. M. Martirez, S. Kim, E. H. Morales, B. T. Diroll, M. Cargnello, T. R. Gorden, C. B. Murray, D. A. Bonnell, and A. M. Rappe, J. Am. Chem. Soc. **137**, 2939 (2015).

[28] J. L. G. Fierro, ed., *Metal Oxides: Chemistry and Aplications* (CRC Press Tayler & Francis Group, 2006), chap. 19 - 20, pp. 595 – 660.

[29] S. C. Roy, O. K. Varghese, M. Paulose, and C. A. Grimes, ACS Nano **4**, 1259 (2010).

[30] A. Kudo and Y. Miseki, Chem. Soc. Rev. **38**, 253 (2009).

[31] C. Dette, M. A. Pérez-Osorio, C. S. Kley, P. Punke, C. E. Patrick, P. Jacobson, F. Giustino, S. J. Jung, and K. Kern, Nano Lett. **14**, 6533 (2014).

[32] C.-W. Lee, R. K. Behera, S. Okamoto, R. Devanathan, E. D. Wachsman, S. R. Phillpot, and S. B. Sinnott, J. Am. Ceram. Soc. **94**, 1931 (2011).

[33] C.-W. Lee, R. K. Behera, E. D. Wachsman, S. R. Phillpot, and S. B. Sinnott, Phys. Rev. B **83**, 115418 (2011).

[34] T. Hikita, T. Hanada, M. Kudo, and M. Kawai, J. Vac. Sci. Technol. A **11**, 2649 (1993).

[35] U. Diebold, Surf. Sci. Rep. **48**, 53 (2003).

[36] J. Ihm, A. Zunger, and M. L. Cohen, J. Phys. C **12**, 4409 (1979).

[37] P. Giannozzi, S. Baroni, N. Bonini, M. Calandra, R. Car, C. Cavazzoni, D. Ceresoli, G. L. Chiarotti, M. Cococcioni, I. Dabo, et al., J. Phys.: Condens. Matter **21**, 395502 (2009).

[38] A. M. Rappe, K. M. Rabe, E. Kaxiras, and J. D. Joannopoulos, Phys. Rev. B Rapid Comm. **41**, 1227 (1990).

[39] N. J. Ramer and A. M. Rappe, Phys. Rev. B **59**, 12471 (1999).

[40] J. P. Perdew, K. Burke, and M. Ernzerhof, Phys. Rev. Lett. **77**, 3865 (1996).

[41] C. Broyden, J. Inst. Maths Applics **6**, 76 (1970).

[42] R. Fletcher, The Compter Journal **13**, 317 (1970).

[43] D. Goldfarb, Mathematics of Computation **24**, 23 (1970).

[44] D. F. Shanno, Mathmetics of Computation **24**, 647 (1970).

[45] D. F. Shanno and P. C. Kettler, Mathmetics of Computation **24**, 657 (1970).

[46] M. Cococcioni and S. de Gironcoli, Phys. Rev. B **71**, 035105 (2005).

[47] C. Cramer, W. Tolman, K. Theopold, and A. Rheingold, Proc. Natl. Acad. Sci. USA **100**, 3635 (2003).

[48] M. C. Toroker, D. K. Kanan, N. Alidoust, L. Y. Isseroff, P. Liao, and E. A. Carter, Phys. Chem. Chem. Phys. **13**, 16644 (2011).

[49] J. P. Perdew and M. Levy, Phys. Rev. Lett. **51**, 1884 (1983).

[50] J. F. Janak, Phys. Rev. B **18**, 7165 (1978).

[51] C. J. Fall, N. Binggeli, and A. Baldereschi, J. Phys. Condens. Matter **11**, 2689 (1999).

[52] O. Sinai, O. T. Hofmann, P. Rinke, M. Scheffler, G. Heimel, and L. Kronik, Phys. Rev. B **91**, 1 (2015).

[53] L. Kronik and Y. Shapira, Surf. Sci. Rep. **37**, 1 (1999).

[54] S. M. Sze and K. K. Ng, *Physics of Semiconductor Devices* (Wiley-Interscience, Hoboken, New Jersey, 2006).

[55] M. M. Waegele, X. Chen, D. M. Herlihy, and T. Cuk, J. Am. Chem. Soc. **136**, 10632 (2014).

[56] J. K. Nørskov, J. Rossmeisl, A. Logadottir, L. Lindqvist, J. R. Kitchin, T. Bligaard, and J. H., J. Phys. Chem. B **108**, 17886 (2004).

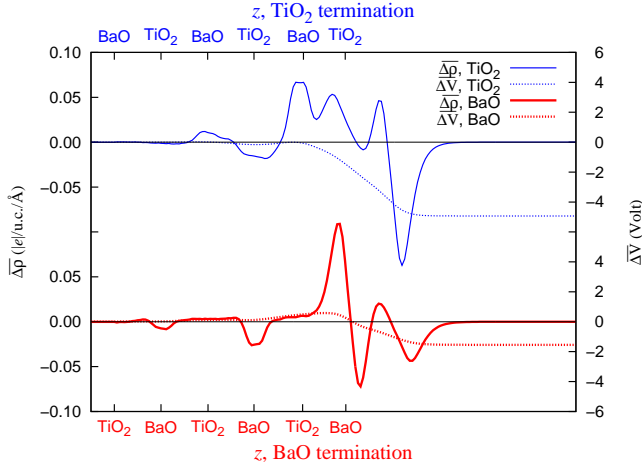[57] J. Rossmeisl, Z. W. Qu, H. Zhu, G. J. Kroes, and J. K. Nørskov, J. Electroanal. Chem. **607**, 83 (2007).

FIG. 6: (Color online) Redistribution of charge ($\overline{\Delta\rho}$) and resultant electrostatic potential ($\overline{\Delta V}$) at the bulk-like $c(2 \times 2)$ BaO- and TiO$_2$-terminated surfaces of BaTiO$_3$. Charge density and potential are averaged across a distance corresponding to the BaTiO$_3$ lattice constant (4.04 Å). Negative charge values represent an excess of electrons.

VI. APPENDIX

A. Surface dipoles at the bulk-like terminations of BaTiO$_3$

Fig. 6 shows the redistribution of charge density associated with the formation of the bulk-terminated BaTiO$_3$

slabs from neutral atoms, and the resultant change of electrostatic potential. We first subtract the charge density of the isolated atoms from that of the slab, and then average the charge density difference over a BaTiO$_3$ unit cell thickness, so that $\overline{\Delta\rho}$ and the $\overline{\Delta V}$ calculated from it asymptote far from the surface to zero and to a constant value, respectively;

$$\Delta\rho(z) = \rho_{\text{slab}}(z) - \sum_i \rho_{X_i}(z - z_i) \qquad (7)$$

$$\overline{\Delta\rho}(z) = \frac{1}{l} \int_{z-l/2}^{z+l/2} \Delta\rho(z - z')dz'. \qquad (8)$$

$\rho_{X_i}(z)$ and z_i are the charge density (averaged in the x,y plane) and the position, respectively, of the i-th isolated atom of type X ($X = $ Ba, Ti and O). The lattice constant (l) of BTO is 4.04 Å in our calculations.

Because more electrons migrate from the subsurface to the TiO$_2$-terminated surface than to the BaO-terminated one, a stronger inward-pointing dipole moment is induced at the former, leading to a more negative ΔV. This difference in surface dipoles is the origin of the band edge differences observed between BaO and TiO$_2$ terminations.

B. Geometric structures of surfaces

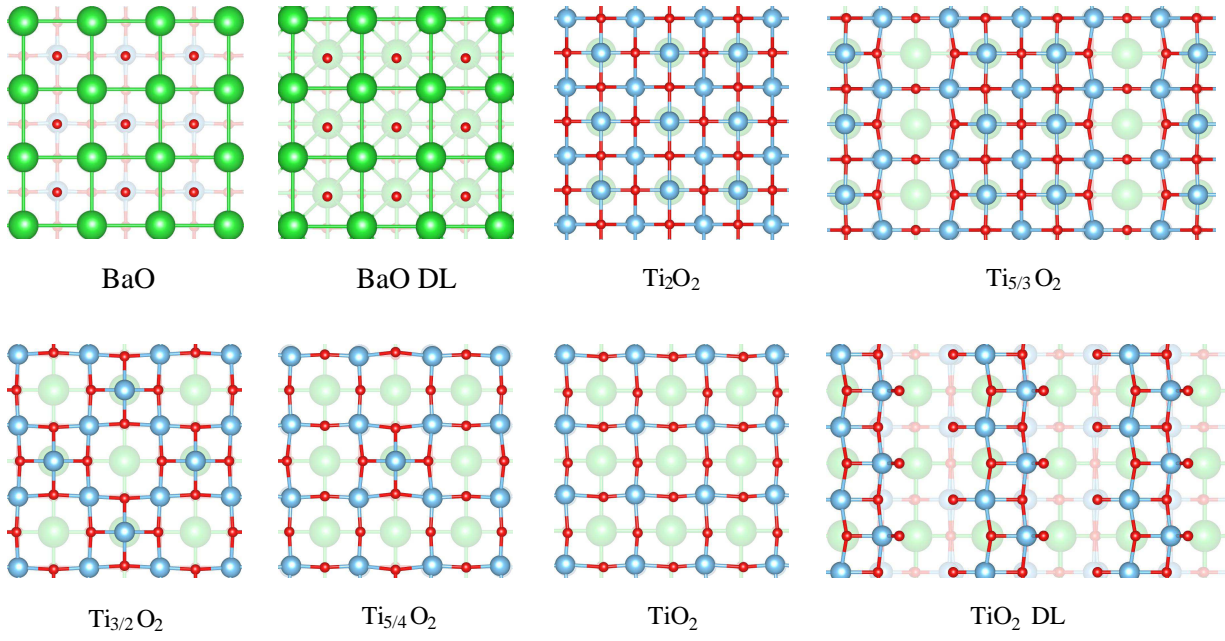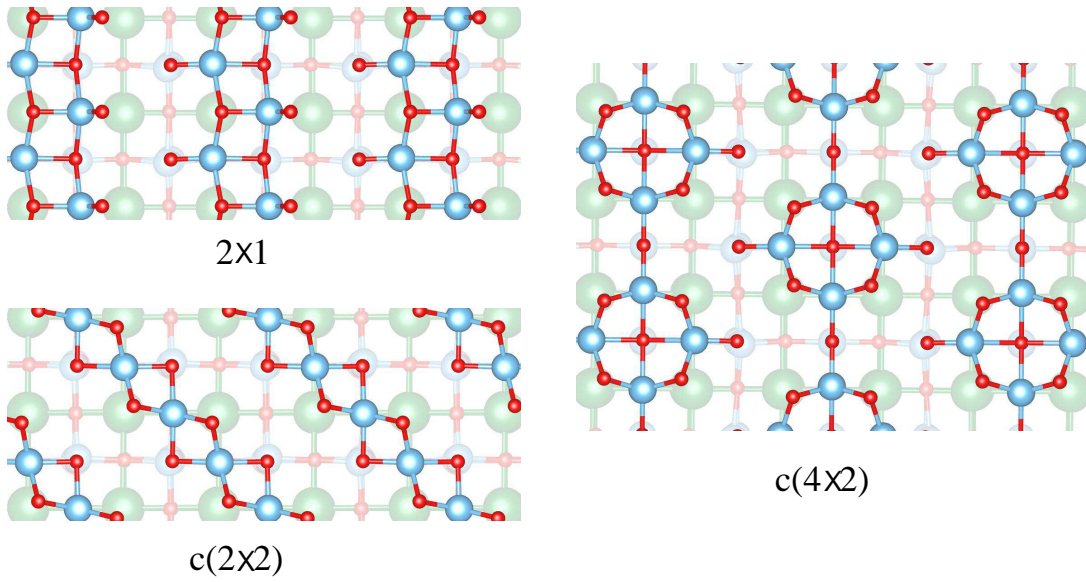FIG. 7: (Color online) Top-view of BaTiO$_3$ (001) surfaces.

FIG. 8: (Color online) Top-view of SrTiO$_3$ (001) TiO$_2$ double-layer structues.

2×1 Ti$_{1/2}$O$_{3/4}$
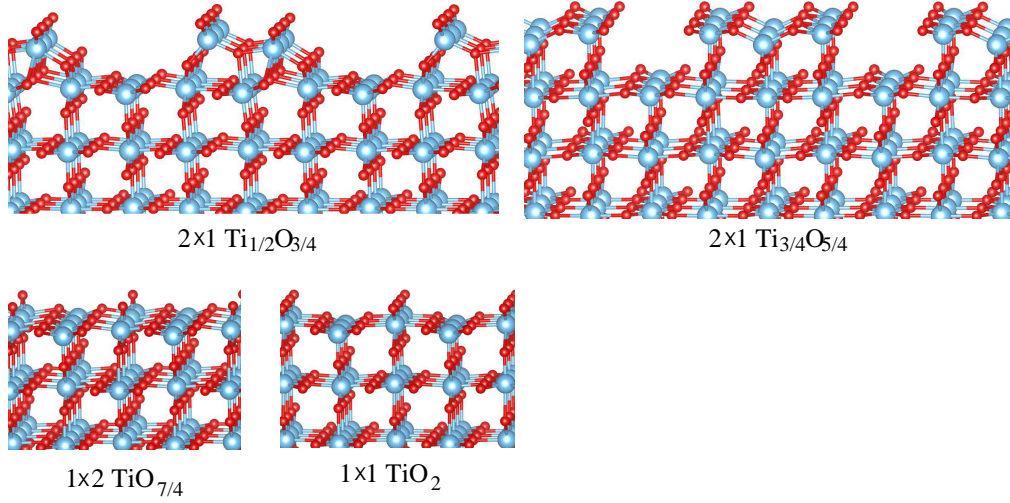
2×1 Ti$_{3/4}$O$_{5/4}$

1×2 TiO$_{7/4}$

1×1 TiO$_2$

FIG. 9: (Color online) Atomic structures of rutile (110).

LaO

LaO$_{3/2}$

LaO$_2$

Fe
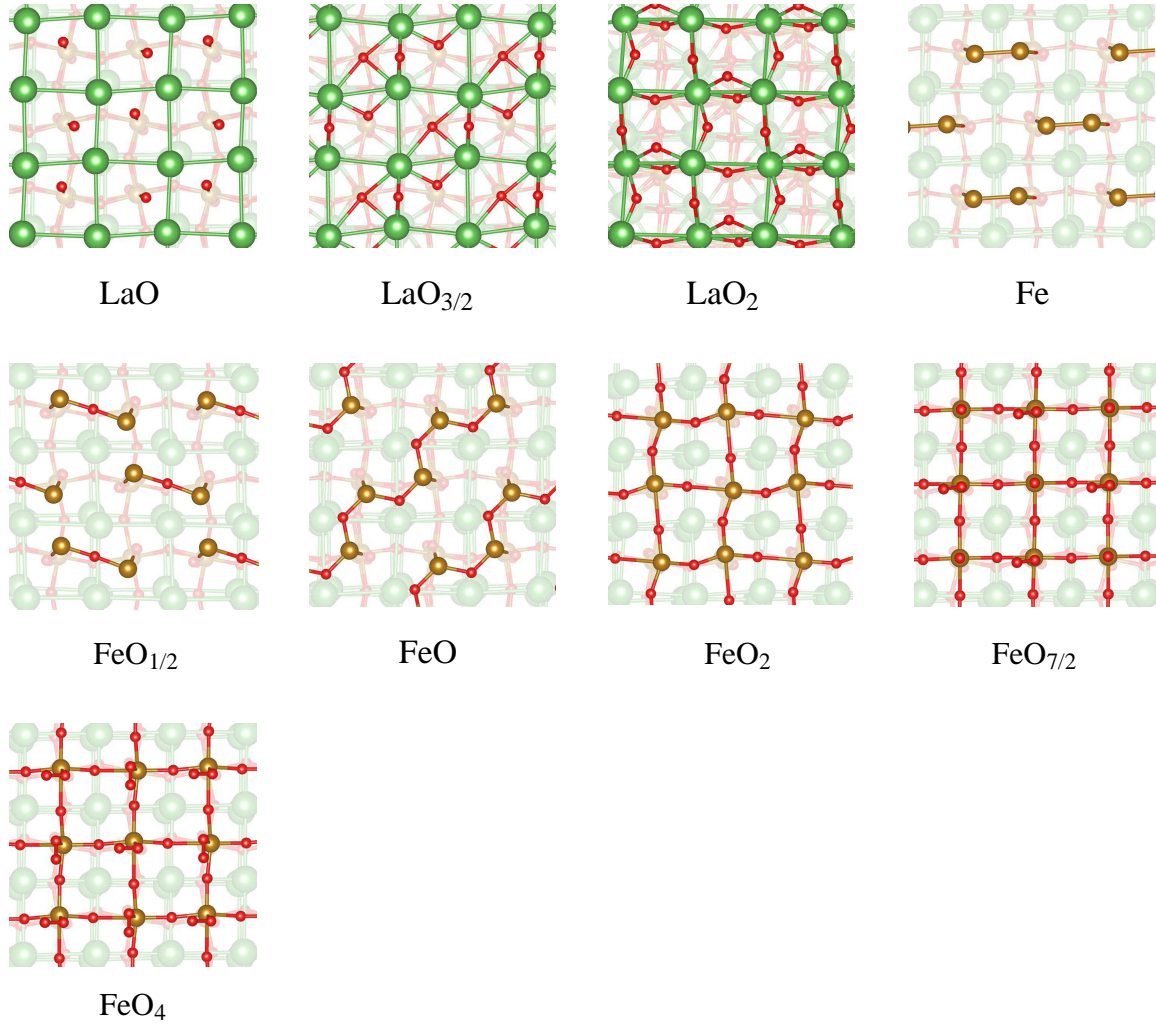
FeO$_{1/2}$

FeO

FeO$_2$

FeO$_{7/2}$

FeO$_4$

FIG. 10: (Color online) Top-view of LaFeO$_3$ (010) surfaces.